RSC Advances

ROYAL SOCIETY OF CHEMISTRY

www.rsc.org/advances

ARTICLE TYPE www. rsc.org/xxxxxx | XXXXXXXX

A Series of Unexpected Ferromagnetic Behavior Based on Surface–Vacancy State: Insight into NiO Nanoparticles with Core–Shell Structure

Zhaolong Yang, Daqiang Gao, Kun Tao, Jing Zhang, Zhenhua Shi, Qiang Xu, Shoupeng Shi and Desheng Xue*

Received Xth XXXXXXXXXX 20XX, Accepted Xth XXXXXXXXX 20XX
First published on the web Xth XXXXXXXXXX 200X
DOI: 10.1039/b000000x

Antiferromagnetic nanoparticles as ultimate low–dimensional materials potentially give novel magnetic properties which differ from their bulk form due to the strong quantum and surface effects. Here, we original propose the observed anomalous ferromagnetic behavior in NiO nanoparticles to the formation of a ferromagnetism particle shell which is oxygen-vacancy related. A novel self-consistent estimation to the saturation magnetization further confirmed our proposal. The samples synthesized by thermal decomposition method exhibit diversely anomalous ferromagnetic behavior, such as hysteresis curves, large coercivities, exchange bias and spin–glass behavior. Large saturation magnetization of 0.536 emu/g exists in the 6 nm NiO sample and it is found to decrease with increasing crystal size. Neither impurity element nor change of valence state has been found in the samples through X–ray photoelectron, X–ray diffraction and selected–area electron diffraction measurements. Remarkably, large amount of oxygen vacancies exist which was verified by X–ray photoelectron spectrum fitting results and Raman spectrum. Post–hydrogen–annealing process strongly elevates ferromagnetic ordering as a result of surface defect enhancement. Moreover, our estimate to the saturation magnetization based on a first principle calculation results is in agreement with the experimental conclusion, which reveals significance of surface states to mediate anomalous magnetic properties in low–dimensional antiferromagnetic materials.

1 Introduction

Since it was firstly reported the anomalous magnetic susceptibility in antiferromagnetic (AF) nanoparticles by Richardson and Milligan,[1] great effort has been paid to understand the nature of those unexpected phenomena.[2–4] Subsequent years, ferromagnetic–like behaviors were found in a growing number of AF nanomaterials.[5–7] Nevertheless, the mechanism of these different physical properties remains debatable theoretically. Many views were proposed to the observed ferromagnetism (FM), such as different site occupancy of magnetic ions, chemical valence change, presence of superparamagnetic clusters, or vacancy related uncompensated surface spins.[2,4,8–10] Among these, it is highly probable that new surface or interface states will be formed and play a role in inducing FM order when the materials turn down–sizing into nanodimensions.[11,12] A series of experiment results show that the size of low–dimensional systems, such as film thickness or diameter of nanoparticles would influence the observed FM due to the high surface to volume ratio and alternation in the electronic states.[5,13,14] It is also supported by theoretical works which show the effects of surface curvature, quantum confinement, and size on various properties of nanocrystals.[15,16] AF materials attract much attention because they are pinning layers among exchange biasing which is already widely used in magnetoresistive read heads and, furthermore, has been proposed as candidates for generating magnetic recording media with high thermal stability.[17] Therefore, understanding and controlling the FM order in those systems is important in both theory and future applications.[18]

NiO has been widely investigated because of the excellent and multifunctional magnetic properties. A rather high Néel temperature (T_N) and Mott–Hubbard insulator character distinguishes NiO from other AF materials.[19,20] The presence of anomalous magnetic properties in NiO nanomaterials was first reported in 1950s.[1] Néel first proposed the 2–sublattices model which is accepted for bulk NiO to explain the observed puzzlements. The net moment of small AF nanoparticles was attributed to the uncompensated surface spins which the number of magnetic spins oriented in opposite directions are not equal.[2] However, further experimental facts show that the saturation magnetizaition was much larger than the calculated value in terms of 2–sublattices AF ordering.[21,22] Later, multi-

Key Laboratory for Magnetism and Magnetic Materials of MOE, Lanzhou University, Lanzhou 730000, P. R. China. Fax: +86-0931-8914160; Tel: +86-0931-8912237; E-mail: xueds@lzu.edu.cn

sublattice spin configuration was suggested to the observations in those systems which allows for more net moments.[10] Another mechanism based on the origin of moments, which was widely accepted by researchers, is the presence of Ni^{3+} ions within the NiO lattice. The Ni^{3+} ions have a low–spin $3d^7$ configuration which possess different magnetic moment from Ni^{2+}.[23,24] If the Ni^{3+} ions are concentrated at the particle surface, the net moments will be considerable. This assumption seemed plausible since NiO nanoparticles prepared by decomposition at low temperature is always nonstoichiometric.[9,25,26] But recent X–ray photoelectron spectroscopy (XPS) and X–ray absorption spectroscopy results do not support the existence of Ni^{3+} in NiO nanostructures.[27,28] Other views such as that defects bear the brunt of the moment origin, inevitable metallic nickel cluster causes the FM, have also been proposed.[2,21] Whereas, the controversy of FM origin is still open and novel properties such as exchange bias and spin–glass (S-G) behavior are discovered. This motivated us to explain the unexpected FM of NiO nanoparticles, and the surface oxygen vacancy is confirmed to be the dominant contribution of the FM through both experimental analysis and first principle calculation.

2 Experimental and calculation section

The synthetic product is obtained by a simple thermal decomposition method. In a typical procedure, the precursor $Ni(OH)_2$ was prepared by coprecipitation with nickel nitrate $[Ni(NO_3)_2{\cdot}6H_2O]$ and sodium hydroxide (NaOH). Briefly, 0.5 mol/L nickel nitrate and 10 mol/L sodium hydroxide was dissolved in deionized water respectively. After stirring for 30 mins, the sodium hydroxide solution was added dropwise to the nickel nitrate solution under vigorous stirring. The precipitation occurred immediately and changed the reaction solution to green. During the reaction, pH of the solution increased gradually and precipitated completely until pH = 8. After stirring for 1 hr, the obtained products were separated by centrifugation and washed with deionized water for several times until impurity ion was free from $Ni(OH)_2$. Then the precursor was dried at 60 °C in air for 12 hrs. NiO nanoparticles were obtained by decomposing the $Ni(OH)_2$ precursor in argon at different temperatures. To hold the annealing details, TG and DTA were measured for the precursor (not shown) in argon atmosphere, indicating that $Ni(OH)_2$ is completely decomposed into NiO and H_2O above 300 °C. So the annealing temperatures were chosen from 300 to 700 °C every 100 °C. All the samples were annealed for 2 hrs in argon with a gas flow rate of 40 standard cubic centimeters per minute (SCCM), and named as S300, S400, S500, S600, and S700, respectively.

The crystal structure and size was analyzed from their X–ray diffraction (XRD; X'Pert PRO PHILIPS with Cu K_α radiation, Almelo, The Netherlands) patterns. Microstructures of the samples were characterized using a transmission electron microscope (TEM; Tecnai TMG2F30, FEI, Hillsboro, OR, USA) and high–resolution TEM (HRTEM) equipped with selected–area electron diffraction (SAED). The measurements of magnetic properties were performed using a Quantum Design MPMS magnetometer based on a superconducting quantum interference device (SQUID; San Diego, CA, USA) and vibrating sample magnetometer equipped with high temperature chamber (VSM; VSM Model EV9, MicroSense, LLC, Massachusetts, USA). Raman scattering spectra were obtained using a Jobin–Yvon LabRam HR80 spectrometer (Horiba Jobin Yvon Inc., Edison, NJ, USA) with a 532 nm line of Torus 50 mW diode–pumped solid–state laser under backscattering geometry. The chemical bonding state and compositions of the products were determined by XPS (VG Scientific ESCALAB–210 spectrometer, East Grinstead, UK) with monochromatic Mg K_α X–rays source (1,253.6 eV). The thermogravimetric and differential thermal analysis (TG–DTA; DuPont Instruments 1090B, Parkersburg, VA, USA) was employed to obtain the thermal decomposition details of precursor.

Our calculations are based on the density functional theory (DFT) implemented in VASP code within the generalized gradient approximation (GGA) due to Perdew, Burke and Ernzerhof (PBE). In order to describe the ion core electrons, the projector augmented wave (PAW) potentials are used. The electronic states are expanded in terms of plane waves with the number restricted by maximal kinetic-energy cutoff of 520 eV. All parameters in calculations are chosen to converge the total energy to 1.0×10^{-5} eV. A $7\times7\times1$ Monkhost and Pack grid points were used for geometry optimization. The geometry was optimized without any symmetry constraint until all residual forces on each atom were less than 0.01 eV/Å. Since the transition metal oxides are strongly correlated materials, the on-site Coulomb repulsion parameter, the so-called Hubbard U, should be taken into account. We perform all calculations using GGA+U method with the parameter U equals to 4.6 eV, which is self-consistently calculated from the linear response approach.[29] The magnetic moment of the Ni ions is correctly described within the present GGA+U approach, which gives a value of about 1.7 μ_B (Bohr magneton) well within the experimental range of values ranging from 1.64 and 1.9 μ_B, better than the value of 1.55 μ_B obtained within GGA.[30,31]

3 Results and discussion

The XRD pattern for the $Ni(OH)_2$ precursor is presented in Fig. 1, and all the peaks are consistent with hexagonal structure $Ni(OH)_2$ (JCPDS card no. 14–0117). After annealing, the precursor was turned into rocksalt structure of NiO (JCPDS card no. 47–1049). Absence of any other peak suggests that

there is no secondary phase present. Using the Scherrer formula for the full width at half–maximum of the main peaks, the average crystal size was calculated to be around 6.1, 11.3, 19.8, 46.5, and 79.8 nm for the samples of S300 to S700 (inset of Fig. 1), respectively. It can be understood that the crystalline size increases as the increasing annealed temperature. To characterize the microstructure and morphology of different NiO samples, TEM analysis was carried out and the results shown in Fig. 2. Obviously, all the products disperse well and mean particle size gradually gets larger with increasing annealed temperature. Representative particle size read from Fig. 2(b) and (c) matches the mean crystal size calculated from XRD patterns well. Even in the smallest particle sample S300, the clear atom arrangement can be found and the corresponding lattice spacing is 0.21 nm equaling to the interplanar spacing of rocksalt NiO in (200) plane [inset of Fig. 2(a)]. The homologous SAED patterns of S300, S500 and S700 are depicted in Fig. 2(d)–(f). The diffraction patterns change from rings to shiny spots with the grains grown and all can be indexed to rocksalt NiO where the agreement with the XRD pattern is excellent.

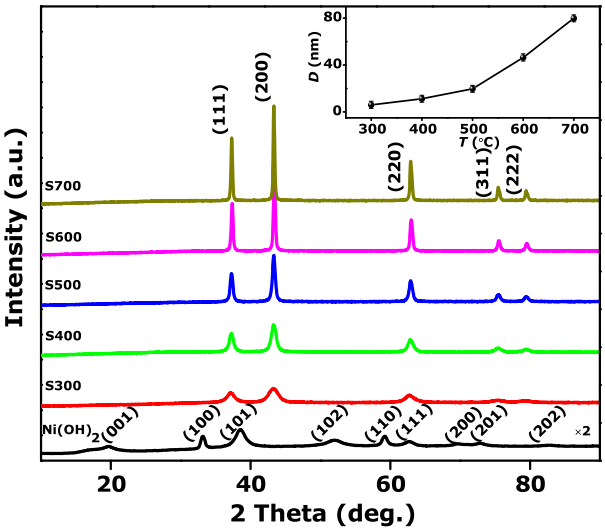

Fig. 1 XRD patterns of $Ni(OH)_2$ precursor and samples S300 to S700. The inset shows average crystal size of samples S300 to S700 calculated by the Scherrer formula.

Magnetic property of precursor $Ni(OH)_2$ was studied firstly, the magnetization curve as a function of applied magnetic field (M–H) was measured at 300 K. As shown in the inset of Fig. 3(a), no hysteresis loop is observed and only paramagnetic (PM) signal is detected, which indicates the precursor is non–ferromagnetism. Then the M–H curves were measured for samples S300 to S700 and displayed in Fig. 3(a) under a maximum applied magnetic field of 70 kOe at 300 K using SQUID. Capsules free from metallic impurity were used as

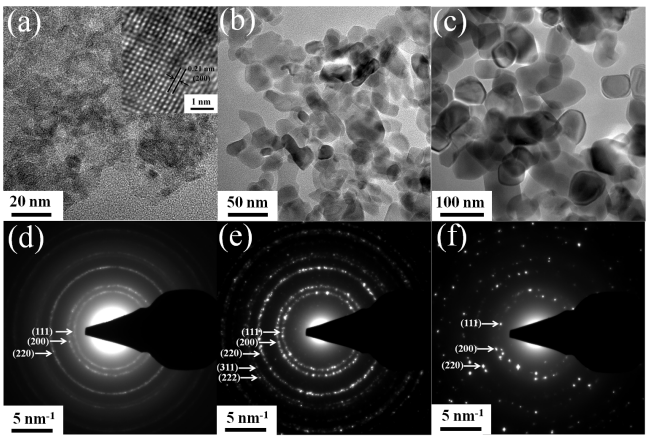

Fig. 2 Morphological characteristics of NiO nanoparticles. (a-c) TEM images of samples S300, S500 and S700. Inset of (a) shows HRTEM image of S300. (d-f) The corresponding SAED patterns of samples S300, S500 and S700.

sample holders. Note that the bulk NiO is AF material which should only show PM signal, but our samples clearly exhibit FM hysteresis loops. Moreover, FM signals strongly depend on the crystal size of samples, the strongest saturation magnetization (M_s) reaches 0.536 emu/g in the smallest grain size sample S300. Those phenomena reflect that the room temperature (RT) FM is nature of NiO nanoparticles and size effect plays a crucial role in performing FM signals. In addition, it can be seen from Fig. 3(a) that the AF susceptibility changes faintly with the decreasing crystal size. Combining with that the nanoparticles remain the lattice structure of bulk NiO, it could conclude that main of the whole particle would still maintain AF. This motivated us to consider NiO nanoparticles present in a core–shell structure.[7,13,14,32] FM originates from surface of the crystal grains meanwhile the core still remains AF. The M–H curves for sample S300 measured at different temperatures are shown in Fig. 3(b). The PM signals were subtracted and magnetization becomes saturated at rather large applied field about 60 kOe. It can be seen that the M_s decreases as the temperature increases from 10 to 300 K revealing typical signature of a nominal FM–like material. The coercive field increases in a monotonic fashion from a value of 1.93 kOe at 300 K to 6.98 kOe at 10 K. The considerable large hysteresis may be attributed to the pinning effect from AF core to FM shell occurring at the interface.[33]

To confirm the hypothesis above, we measured exchange bias of S300. Both zero–field–cooled (ZFC) loop and field–cooled (FC) loop at 10 K are shown in Fig. 3(c). The first measurement was taken after demagnetization at 300 K and then cooled down without applied field to the measurement temperature (10 K), and in second run the measurements were taken after 70 kOe FC process. Exchange bias field (H_{eb}) can

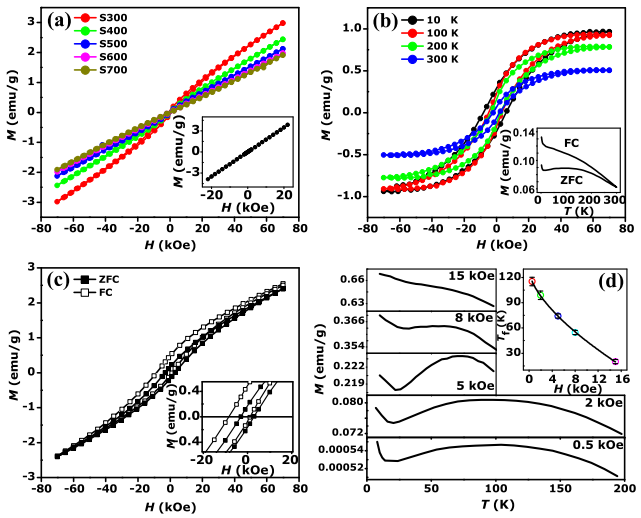

Fig. 3 (a) *M–H* curves of samples S300 to S700 which were measured at RT by SQUID. The inset shows RT *M–H* curve of $Ni(OH)_2$ precursor. (b) *M–H* curves for sample S300 at different temperatures, where the PM signals have been deduced. ZFC–FC curve for sample S300 in the temperature range of 2 to 300 K at 500 Oe are shown in the inset. (c) ZFC and FC hysteresis loops measured at 10 K for sample S300 which taken after zero field and 70 kOe field cooled processes respectively. The inset shows a magnified view of the low–field data. (d) ZFC curves of sample S300 by applying a range of different fields. The fitting curve of freezing temperature T_f (read from ZFC curves) versus H is shown in the inset.

be defined as the amount of the loop displacement and coercivity (H_c) as the half–width of the loop. Generally, in an exchange biased system, loop displacement can be observed in the limit where the coupling energy between FM and AF phase is weak compared to the anisotropy energy of the AF phase. Otherwise, the FM and AF spins rotate simultaneously, resulting in enhancement of H_c. In our case, the exchange bias exists distinctly: loop displacement H_{eb} is 3.65 kOe. Besides, shift of loop is more pronounced than the increase of H_c (increased 1.80 kOe), proving the coupling energy between two phases is weak. Those may be due to the low content of FM phase.[12,34] Through above analysis, more details could be confirmed: NiO nanoparticles are in a coexistence state of AF and FM phase, FM signals come from the shell of the whole grain; the coupling energy between AF core and FM shell is weaker than the AF anisotropy energy. The inset of Fig. 3(b) depicts temperature–dependent ZFC–FC magnetization curves from 2 K to 300 K at 500 Oe. The dividable curve reveals that the magnetization reversal is irreversible for the NiO nanoparticles and Curie temperature (T_C) of the sample is above 300 K. When cooling down from 300 K, both ZFC and FC curves follow a similar trend, that is, the susceptibility increases slowly; until a broad peak at 115 K appears in ZFC curve. Meanwhile, the FC curve monotonously increases in the measured temperature range. Controversy still remains in the magnetic properties around the susceptibility cusp, it is not clear whether the system goes through a sharp phase transition or a progressive freezing of the spins. There were reports suggesting that the temperature peak represents a superparamagnetic behavior of the interacting particles, while other researchers believe that the peak symbolizes a freezing temperature (T_f) due to the uncompensated surface moments in a SG system.[9,26,35,36] As a consequence, some methods had been suggested to identify the classification of peaks.[9,35–38] For SG behavior, T_f peak would shift towards lower temperature side with the increasing magnetic field, the relationship between cusp temperature T_f and applied field H depicts as a function of $T_f/T_0 \propto 1 - (H/J)^{2/3}$.[37] According to this, the measurement of ZFC curves was performed at different applied field for S300. The results are shown in Fig. 3(d) and applied field was chosen as 0.5, 2, 5, 8, and 15 kOe respectively. It can be seen that the broad peak has been suppressed and shifts obviously to the lower side when the field becomes larger. The fitted curve of cusp temperature versus applied field H used the functional form above with unfixed index is shown in inset of Fig. 3(d). The best fitting function is $T_f = -0.239 \times H^{0.636} + 128$, where the index of applied field H is 0.636 which is close to 2/3 indicating the expected SG behavior present in our sample.

Investigation of temperature dependence magnetization measurements above RT was performed on S300 and the results are shown in Fig. 4. In a typical measurement, sample powders were pressed into slice and covered with alumina ceramics to stick on the quartz sample holder. The alumina ceramics and sample holders are non–ferromagnetism. It can be seen that the magnetization versus temperature (*M–T*) curve [Fig. 4(a)] shows rapid decay of magnetization from the initial temperature region with the increasing measured temperature, then a sharp susceptibility peak appears near 250 °C (523 K) which indicating clear Néel transition of AF NiO. Since then, the magnetization decreases continuously without obvious T_C of phase transition from FM to PM in measured region. Fig. 4(b) shows the *M–H* curves measured at 120, 200 and 450 °C, which are before and after the Néel transition respectively. M_s decreases to 0.0085 emu/g at 450 °C but the curve still shows clearly FM hysteresis even the AF ordering has already vanished at this temperature. It is noteworthy that the T_C of S300 is higher than that of metallic nickel (T_C = 358 °C; 631 K) which indicates that the FM is due to the intrinsic character of NiO nanoparticles rather than presence of metallic nickel cluster. Besides, Since the weaker exchange coupling between FM and AF interface at high temperature, the value of H_c drops from 1.93 kOe at RT to 132 Oe at 120 °C. The results above give an implication that FM ordering could exist independent

of AF phase.

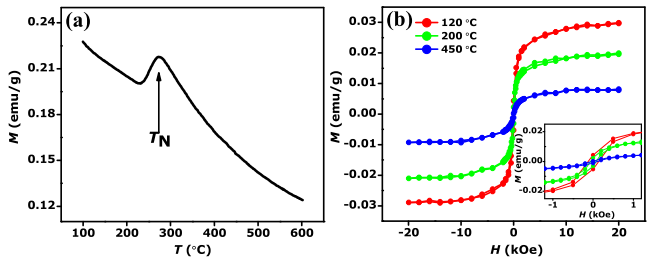

Fig. 4 (a) *M–T* curve for sample S300 which were investigated in the temperature range from 100 to 600 °C by VSM under the applied field of 20 kOe. (b) *M–H* curves for the sample S300 measured at 120, 200 and 450 °C; where the PM signals have been deduced. The inset shows the amplifying *M–H* part in the low–field.

The bonding characteristics and composition of the NiO nanoparticles were captured by XPS to investigate whether the observed FM in the samples is originated from metallic nickel cluster, valence change of Ni^{2+}, or anion/cation vacancies. Representative spectra of S300 and S700 are shown in Fig. 5(a). The result shows that only Ni, O, and C elements are presented in XPS survey, where the standard C 1*s* peak at 284.6 eV was used as a reference for correcting the shifts. None of other FM element contamination or metallic nickel has been found. The Ni $2p_{3/2}$ photoemission line shape shows a multi–peak structure [Fig. 5(b)] which has been widely discussed in previous work.[27,28,39,40] The spectra can be fitted by three peaks corresponding to the binding energies of 854.0, 855.8 and 861.2 eV. It is accepted that the binding energy peak located at 854.0 eV (Ni_a) represents the Ni^{2+} cation in octahedral site of NiO_6 cluster, an additional shoulder peak separated by 1.8 eV (855.8 eV; Ni_b) at higher binding energy corresponding to the Ni^{2+} in NiO_5 cluster which is oxygen vacancy related at surface [The diagrams are shown in inset of Fig. 5(b)].[39] Another satellite peak of Ni $2p_{3/2}$ can be found at 861.2 eV. The mixture of bulk and surface components form the experimental Ni $2p_{3/2}$ spectrum. Calculation on the area ratio of Ni_b to Ni_a shows that the relative intensity decreases from 1.54 to 1.32 for samples S300 and S700; that reveals the concentration of surface oxygen vacancies reduced with increasing annealing temperature. Meanwhile, O 1*s* core level spectra can be fitted by two peaks [Fig. 5(c)] which lower binding energy peak located at 529.3 eV (O_a) is attribute to O^{2-} ions in NiO_6 cluster, the higher binding energy peak located at 531.0 eV (O_b) can be assigned to the O^{2-} ions in oxygen-deficient regions close to the NiO_5 cluster. As can be seen in Fig. 5(c), O_b peak is always present and calculated relative intensity of O_a decreases from 0.94 to 0.67 as the crystal size increases. Calculation of the relative chemical compositions for S300 reveals a Ni:O molar ratio of ~ 1:0.89 at surface. The above results could be interpreted as oxygen vacancies present in all samples, and its concentration increased with increased surface–to–volume ratio. More importantly, as decreasing the crystal size, the larger relative area of Ni_b and O_b is, the larger M_s is. Oxygen vacancies have possibility to contribute to the magnetization due to cancellation of superexchange interaction between adjacent Ni^{2+} which changes the spin-polarized state of valence electrons, eventually making the shell of NiO nanoparticles possess observable FM signals.

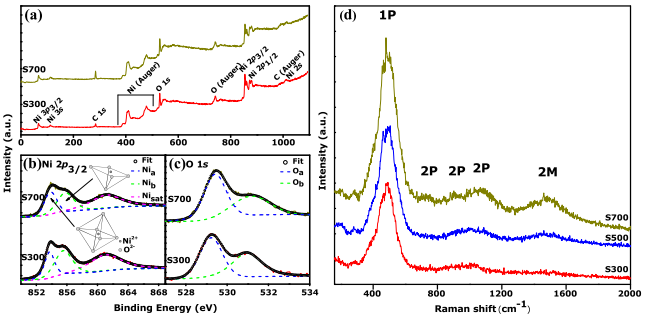

Fig. 5 (a) XPS survey spectra of samples S300 and S700. (b, c) High–resolution scans of Ni $2p_{3/2}$ and O 1*s* for samples S300 and S700. (d) Raman spectra acquired from samples S300, S500 and S700.

Additional structure information of NiO nanoparticles was obtained by Raman spectroscopy. Fig. 5(d) shows the RT Raman spectra of S300, S500 and S700. All the samples show five peaks in the probed region of 200 – 2000 cm^{-1}. The first four peaks origin from lattice vibration which correspond to one–phonon (1P) transverse optical (TO) and longitudinal optical (LO) modes at 495 cm^{-1}, two–phonon (2P) 2TO modes at 730 cm^{-1}, TO + LO at 906 cm^{-1} and 2LO modes at 1080 cm^{-1}, respectively.[41–43] Generally, the intensity of one–phonon scattering increases significantly when NiO is defect–rich or due to the surface effect.[41] Note that the disorder–induced 1P peaks at about 495 cm^{-1} in our samples have rather large intensity, which reveals that more vacancies are introduced when the grain size turns into nanoscale. The last peak at 1486 cm^{-1} is due to the two–magnon (2M) scattering which can be observed at RT because of the high T_N.[43] 2M Raman scattering in bulk NiO involves Brillouin zone edge magnons which interact weakly with phonons and the width of Raman lineshape is usually rather narrow.[44] However, the 2M Raman response in our NiO nanoparticles experiences significant broadening and weakening, even vanished in 6 nm crystal size sample S300. Those indicate a decrease of AF spin correlations for smaller size NiO nanoparticles.[41,45]

Until now, the possibility of present contamination and metallic nickel has been already excluded, the observed FM for the NiO nanoparticles must be an intrinsic property of this material. As mentioned before, Raman spectroscopy results give us a revelation that there are large amounts of vacancies

in our samples which are, further determined by XPS fitting results, oxygen vacancies. To confirm whether the RT FM in NiO samples is oxygen vacancy related, post–hydrogen annealing was performed at 170 °C in different ratios of argon and hydrogen for the as–prepared sample S300. It is well known that the hydrogen annealing for oxides can efficiently remove surface oxygen to create more structural defects.[46–49] The increased temperature enhances the reducibility of hydrogen. The active hydrogen molecules unite with the oxygen atoms which loacted at the particles surface, and remove the oxygen atoms by break the Ni–O bonds. We chose the annealing temperature below 550 K to avoid the formation of metallic nickel.[2] The percentages of hydrogen in total flow rate (50 SCCM) were 2%, 10%, 20%, and 50%. Annealing temperature was kept constant for 4 hrs and then cooled naturally. The products named S300H2, S300H10, S300H20, and S300H50, respectively. Variational M_s of post–annealing samples versus ratios of hydrogen are shown in Fig. 6(a). The inset is the resulting *M–H* curves, where the PM signals have been subtracted. For direct comparison, the data of as–prepared sample S300 are also included as beginning. It can be seen that M_s immediately increased from 0.536 to 0.573 emu/g after post–annealing even only 2% hydrogen ratio in the mixture atmosphere. Following the raising of hydrogen ratio, M_s increases continuously and finally reaches 0.638 emu/g. From the Raman results of S300 and S300H50 [Fig. 6(b)], the intensity of vacancy–induced 1P peak turns stronger after post–hydrogen annealing which illustrates concentration of oxygen vacancy indeed increases after annealing process. Meanwhile, XPS measurements for S300 and S300H50 give the similar results, shown in Fig. 6(c) and (d). From the Ni $2p_{3/2}$ and O 1*s* fitting results, relative area of Ni_b and O_b peaks increases 18% and 25% respectively after hydrogen annealing which indicate that more oxygen vacancies were introduced into the sample. In addition, none of Ni^{2+} has been reduced into metallic nickel. Generally, mild hydrogen reduction can introduce oxygen vacancies effectively by broke chemical bond between oxygen atoms and cations. Those additional oxygen vacancies and/or increased shell thickness would finally enhance the M_s.

To further understand the FM ordering in NiO nanoparticles, we intentionally simplified the problem drastically, first-principle calculations based on density functional theory were carried out. The oxygen vacancies are present through the experimental results, so the influence of the oxygen vacancy on magnetic properties of the NiO nanoparticle was investigated. We built a NiO slab which has 5 layers of NiO slice with 8 Ni and 8 O atoms in each layer. Two bottom layers of the slab are fixed and all the other atoms are fully relaxed. The NiO slab is separated by 8 layers of vacuum from neighboring supercell. The calculation process assumed a $Ni_{40}O_{39}$ supercell containing one vacancy of oxygen at the surface. Introducing such a defect leads to a surface oxygen vacancy concentration of about 12.5 at.%. Fig. 7(a) shows the total density of state (DOS) of the supercell (for the convenient comparing, we divided the total DOS by the number of Ni atoms), and the DOSs of the nearest and next nearest neighbor Ni atoms located around the oxygen vacancy. The results indicate that one vacancy of oxygen carries a total net magnetic moment of 0.104 μ_B [Fig. 7(a)]. This confirms oxygen vacancies can indeed produce FM in AF NiO nanoparticles. To further examine of the origin and distribution of the net moment, the difference charge density distribution calculations were performed. For the case of oxygen vacancy, in Fig. 7(b), the results show that the contribution to magnetism is mostly from the four nearest neighbor Ni atoms and the next nearest neighbor Ni atoms only offer little contribution to the total net moment. Based on the above results, we performed an estimation to the macroscopic moment of NiO nanoparticles. To estimate the M_s, samples S300 to S700 were taken into consideration and, for simplicity sake, some assumptions have been put forward: (I) the samples consist of spherical particles with uniform size; (II) the concentration of oxygen vacancy uses the calculation value, 12.5%, which coincides with the relative chemical composition result from XPS measurement; (III) under the saturated field, the net moment arranged parallel to the applied field. The estimation process is described by the following equation:

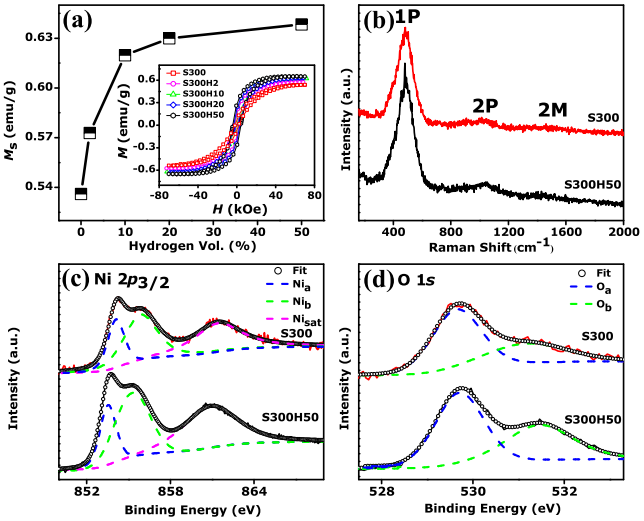

Fig. 6 (a) Variation of M_s versus volume percentage of hydrogen in post–annealing atmosphere for sample S300. *M–H* curves of the post–annealing samples are shown in the inset where the PM signals have been subtracted. (b) Raman spectra of the as–prepared sample and S300H50. (c, d) Ni $2p_{3/2}$ and O 1*s* core level XPS data measured for samples before (S300) and after (S300H50) post–annealing process.

$$M_s = \frac{\mu_{NP}}{m_{NP}} = \frac{n_{shell} v_O \mu_O}{n_O(\frac{M_O + M_{Ni}}{N_A})} \quad (1)$$

$$\frac{n_{shell}}{n_O} = \frac{V_{shell}}{V_{NP}} = \frac{\frac{4}{3}\pi R^3 - \frac{4}{3}\pi(R - r_{shell})^3}{\frac{4}{3}\pi R^3} \quad (2)$$

where μ_{NP} is the saturated moment of each nanoparticle, m_{NP} is the mass of each nanoparticle, n_{shell} is the number of oxygen atoms in FM shell, v_O is the oxygen vacancy concentration, μ_O is the magnetic moment of each vacancy carried, M_{Ni} and M_O are the molar mass of nickel and oxygen, N_A is the Avogadro constant, n_O is the number of oxygen atoms in a whole particle, V_{shell} and r_{shell} are the volume and thickness of shell, V_{NP} and R are the volume and radius of the nanoparticle. Substitute equation (2) into equation (1):

$$M_s = \frac{v_O \mu_O N_A}{M_O + M_{Ni}}[1 - (1 - \frac{r_{shell}}{R})^3] \quad (3)$$

Among equation (3), v_O=12.5%, μ_O=0.104 μ_B, μ_B=9.27×10^{-21} emu, N_A=6.02×10^{23} mol^{-1}, M_O=16.0 g·mol^{-1}, M_{Ni}=58.7 g·mol^{-1}, r_{shell}=1.20 nm. The shell thickness of the nanoparticles are read from a HRTEM image of sample S300 which is shown in Fig. 7(c). To simplify the computations, we assumed that this shell thickness also applied to other samples. The particle radius of each sample was using the average crystal size calculated by Scherrer formula mentioned before (R=3.05, 5.65, 9.90, 23.25 and 39.90 nm, respectively). Through simple calculations, the computational M_s varied with different size samples is shown in Fig. 7(e) (black curve). It can be observed that the changing trend of computational M_s is in agreement with the experimental result [red curve in Fig. 7(e)]. This confirms the size dependent FM signal indeed comes from the shell of the particles. It is noteworthy that the theoretical computation value is always larger than the experimental measuring ones; that is mainly because the impact of thermal disturbance was not taken into account during DFT calculations but the M–H curves of samples S300 to S700 were measured at RT (300 K). Besides, not all of the vacancy induced moment contributes to the FM signal and the rough value of v_O and r_{shell} used in the estimation may also introduce errors in computation results.[50,51] The above analysis further revealed that the observed FM signal is originated from oxygen vacancy induced moment in the particle shell.

Reducing the dimensions of bulk NiO to nanoscale gives us a path to tune its magnetic properties. Through the experiment results mentioned above, when the crystal size is small enough to a certain range (about 6 nm), the NiO nanoparticles exhibit distinct FM signal. Besides, large H_c and exchange bias effect is found by ZFC/FC loop measurements, which indicates coexistence and coupling interaction between

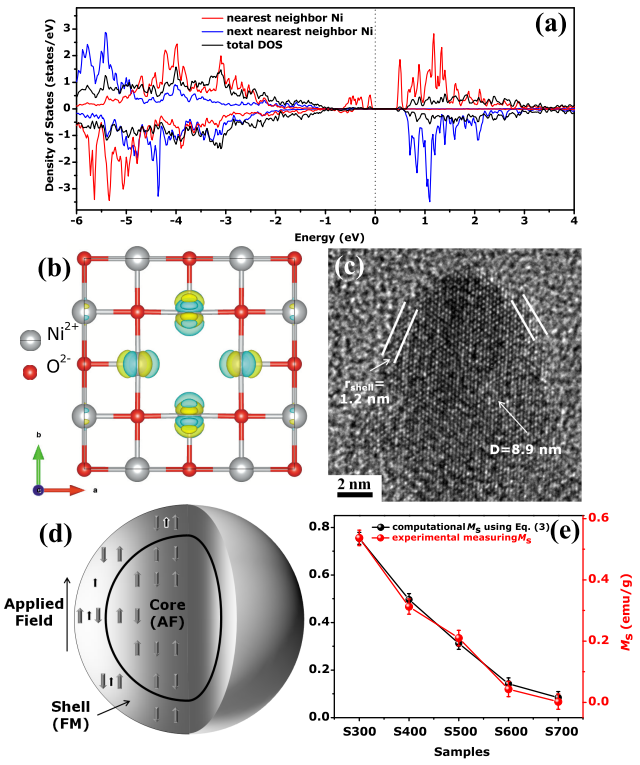

Fig. 7 (a) Total DOS of the $Ni_{40}O_{39}$ supercell (for the convenient comparing, the total DOS was divided by the number of Ni atoms), and DOSs of the nearest and next nearest neighbor Ni relative to the oxygen vacancy. (b) Atomic structure and difference charge density distribution of the supercell. The surface oxygen vacancy concentration in this case is 12.5%. (c) HRTEM image of a S300 nanoparticle. (d) Schematic diagram of the morphological and magnetic structures of the core-shell nanoparticles. (e) The comparison of computational (black curve) and experimental measuring (red curve) M_s for different size samples S300 to S700.

AF core and FM shell. Additional XPS and Raman characterization demonstrates that large amount of oxygen vacancies exists in samples. It can be understood that the crystal defect grows mostly in the boundary and/or surface of grains. With the decreasing size of NiO particles, the ratio of surface–to–volume increases and more vacancies will emerge actually. The chemical bond of Ni–O would be broken by introducing of oxygen vacancies. Such a vacancy carries a moment of 0.104 μ_B which confirmed by first principle calculations. Through a simple estimation, the obtained M_s for S300 to S700 agrees well with the experimental result [Fig. 7(e)]. A schematic diagram for core–shell structure NiO nanoparticles is proposed and shown in Fig. 7(d). The shell contribution is increasing with decreasing particle size and further enhances observed FM. The appearance of exchange bias and large H_c is expected due to pinning effect from AF core to FM shell

in the boundaries. When different particles are in contact, the AF cores are surrounded by a shell of frustrated spins and the interactions between adjacent cores could modulate by shell spins.[32] The alternation of AF ordering regions and shell frustrated spin regions cross many nanoparticles is very similar to the Ruderman-Kittel-Kasuya-Yosida SG models in metallic S-G systems, and this may be the origination of SG behavior in NiO nanoparticles.[32,52–55]

4 Conclusions

In conclusion, we have shown a distinct FM behavior in NiO nanoparticles prepared by the simple thermal decomposition method. The M_s exhibits a clearly monotonous size dependence which is attributed to form a core–shell configuration in nanoparticles. We interpreted the considerable lager H_c and exchange bias in hysteresis loops as pinning effect between AF core and FM shell. XPS and Raman measurements were used to eliminate valence change of Ni^{2+} and systematically investigate the vacancy states. The results show that variation of surface oxygen vacancy concentration is coincident with the change of M_s. Both post-hydrogen-annealing result and estimate of M_s for each sample, based on the first principle calculations, further confirm the above conceptions. Our findings do not only give an insight into the origin of FM observed in NiO nanoparticles but also provide a path to control the FM ordering in AF materials.

ACKNOWLEDGEMENTS

This work is supported by National Basic Research Program of China (Grant No. 2012CB933101), the National Natural Science Fundation of China (Grant No. 51371093, 51202101 and 11034004), Program for Changjiang Scholars and Innovative Research Team in University (Grant No. IRT1251), and Specialized Research Fund for the Doctoral Program of Higher Education (Grant No. 20130211130003).

References

1 J. T. Richardson and W. O. Milligan, *Phys. Rev.*, 1956, **102**, 1289–1294.
2 J. T. Richardson, D. I. Yiagas, B. Turk, K. Forster and M. V. Twigg, *J. Appl. Phys.*, 1991, **70**, 6977–6982.
3 T. Ambrose and C. L. Chien, *Phy. Rev. Lett.*, 1996, **76**, 1743–1746.
4 D. Q. Gao, J. Zhang, J. Y. Zhu, J. Qi, Z. H. Zhang, W. B. Sui, H. G. Shi and D. S. Xue, *Nanoscale Res. Lett.*, 2010, **5**, 769–772.
5 D. P. Dutta, G. Sharma, P. K. Manna, A. K. Tyagi and S. M. Yusuf, *Nanotechnology*, 2008, **19**, 245609.
6 M. Ghosh, K. Biswas, A. Sundaresan and C. N. R. Rao, *J. Mater. Chem.*, 2006, **16**, 106–111.
7 G. J. Yang, D. Q. Gao, J. Zhang, J. L. Zhang, Z. H. Shi, Z. H. Zhu and D. S. Xue, *RSC Adv.*, 2013, **3**, 508–512.
8 L. Li, L. Chen, R. Qihe and G. Li, *Appl. Phys. Lett.*, 2006, **89**, 134102.
9 F. H. Aragón, P. E. N. de Souza, J. A. H. Coaquira, P. Hidalgo and D. Gouvêa, *Physica B*, 2012, **407**, 2601–2605.
10 R. H. Kodama, S. A. Makhlouf and A. E. Berkowitz, *Phys. Rev. Lett.*, 1997, **79**, 1393–1396.
11 A. Sundaresan and C. N. R. Rao, *Nano Today*, 2009, **4**, 96–106.
12 A. Tomou, D. Gournis, I. Panagiotopoulos, Y. Huang, G. C. Hadjipanayis and B. J. Kooi, *J. Appl. Phys.*, 2006, **99**, 123915.
13 M. J. Benitez, O. Petracic, E. L. Salabas, F. Radu, H. Tüysüz, F. Schüth and H. Zabel, *Phys. Rev. Lett.*, 2008, **101**, 097206.
14 A. López-Ortega, D. Tobia, E. Winkler, I. V. Golosovsky, G. Salazar-Alvarez, S. Estradé, M. Estrader, J. Sort, M. A. González, S. Surinach, J. Arbiol, F. Peiró, R. D. Zysler, M. D. Baró and J. Nogués, *J. Am. Chem. Soc.*, 2010, **132**, 9398–9407.
15 A. Soon, X. Y. Cui, B. Delley, S. H. Wei and C. Stampfl, *Phys. Rev. B*, 2009, **79**, 035205.
16 J. M. Wesselinowa, *J. Magn. Magn. Mater.*, 2010, **322**, 234–237.
17 B. Dieny, V. S. Speriosu, S. Metin, S. S. P. Parkin, B. A. Gurney and P. Baumgart, *J. Appl. Phys.*, 1991, **69**, 4774.
18 V. Skumryev, S. Stoyanov, Y. Zhang, G. Hadjipanayis, D. Givord and J. Nogues, *Nature (London)*, 2003, **423**, 850–853.
19 J. McCord and S. Mangin, *Phys. Rev. B*, 2013, **88**, 014416.
20 K. Chakrabarti, B. Sarkar, V. D. Ashok, K. Das, S. S. Chaudhuri, A. Mitra and S. K. De, *J. Appl. Phys.*, 2014, **115**, 013906.
21 H. Bi, S. Li, Y. Zhang and Y. Du, *J. Magn. Magn. Mater.*, 2004, **277**, 363–367.
22 S. A. Makhlouf, H. Al-Attar and R. H. Kodama, *Solid State Commun.*, 2008, **145**, 1–4.
23 W. R. Pease, R. L. Segall, R. S. C. Smart and P. S. Turner, *J. Chem. Soc., Faraday Trans. I*, 1986, **82**, 759–766.
24 L. Qiao and X. Bi, *Europhys. Lett.*, 2011, **93**, 57002.
25 G. Ma, X. Tang, Z. Zhong, H. Zhang and H. Su, *Microelectron. Eng.*, 2013, **108**, 8–10.
26 J. B. Yi, J. Ding, Y. P. Feng, G. W. Peng, G. M. Chow, Y. Kawazoe, B. H. Liu, J. H. Yin and S. Thongmee, *Phys. Rev. B*, 2007, **76**, 224402.
27 D. Alders, F. C. Voogt, T. Hibma and G. A. Sawatzky, *Phys. Rev. B*, 1996, **54**, 7716–7719.

28 L. Sangaletti, L. E. Depero and F. Parmigiani, *Solid State Commun.*, 1997, **103**, 421–424.

29 M. Cococcioni and S. de Gironcoli, *Phys. Rev. B*, 2005, **71**, 035105.

30 H. A. Alperin, *J. Phys. Soc. Jpn.*, 1962, **17**, 12.

31 A. K. Cheetham and D. A. Hope, *Phys. Rev. B*, 1983, **27**, 6964.

32 R. N. Bhowmik, R. Nagarajan and R. Ranganathan, *Phys. Rev. B*, 2004, **69**, 054430.

33 J. B. Yi, J. Ding, Z. L. Zhao and B. H. Liu, *J. Appl. Phys.*, 2005, **97**, 10K306.

34 T. Gredig, I. N. Krivorotov and E. D. Dahlberg, *J. Appl. Phys.*, 2002, **91**, 7760–7762.

35 W. S. Seo, H. H. Jo, K. Lee, B. Kim, S. J. Oh and J. T. Park, *Angew. Chem. Int. Ed.*, 2004, **43**, 1115–1117.

36 M. Ghosh, K. Biswas, A. Sundaresan and C. N. R. Rao, *J. Mater. Chem.*, 2006, **16**, 106–111.

37 J. R. L. de Almeida and D. J. Thouless, *J. Phys. A*, 1978, **11**, 983–990.

38 S. D. Tiwari and K. P. Rajeev, *Phys. Rev. B*, 2005, **72**, 104433.

39 L. Soriano, I. Preda, A. Gutiérrez, S. Palacín, M. Abbate and A. Vollmer, *Phys. Rev. B*, 2007, **75**, 233417.

40 P. Kuiper, G. Kruizinga, J. Ghijsen and G. A. Sawatzky, *Phys. Rev. Lett.*, 1989, **62**, 221–224.

41 N. Mironova-Ulmane, A. Kuzmin, I. Steins, J. Grabis, I. Sildos and M. Pärs, *J. Phys.: Conf. Ser.*, 2007, **93**, 012039.

42 R. E. Dietz, W. F. Brinkman, A. E. Meixner and H. J. Guggenheim, *Phys. Rev. Lett.*, 1971, **27**, 814–817.

43 R. E. Dietz, G. I. Parisot and A. E. Meixner, *Phys. Rev. B*, 1971, **4**, 2302–2310.

44 D. J. Lockwood, M. G. Cottam and J. H. Baskey, *J. Magn. Magn. Mater.*, 1992, **104–107**, 1053–1054.

45 E. Cazzanelli, A. Kuzmin, G. Mariotto and N. Mironova-Ulmane, *J. Phys.: Condens. Matter*, 2003, **15**, 2045–2052.

46 S. H. Liu, H. S. Hsu, C. R. Lin, C. S. Lue and J. C. A. Huang, *Appl. Phys. Lett.*, 2007, **90**, 222505.

47 K. Ogata, T. Komuro, K. Hama, K. Koike, S. Sasa, M. Inoue and M. Yano, *Appl. Surf. Sci.*, 2004, **237**, 348–351.

48 M. Li, S. Ge, W. Qiao, L. Zhang, Y. Zuo and S. Yan, *Appl. Phys. Lett.*, 2009, **94**, 152511.

49 D. Gao, G. Yang, J. Zhang, Z. Zhu, M. Si and D. Xue, *Appl. Phys. Lett.*, 2011, **99**, 052502.

50 T. S. Herng, D.-C. Qi, T. Berlijn, J. B. Yi, K. S. Yang, Y. Dai, Y. P. Feng, I. Santoso, C. Sánchez-Hanke, X. Y. Gao, A. T. S. Wee, W. Ku, J. Ding and A. Rusydi, *Phys. Rev. Lett.*, 2010, **105**, 207201.

51 A. Kaminski and S. D. Sarma, *Phys. Rev. Lett.*, 2002, **88**, 247202.

52 A. Chakrabarti and C. Dasgupta, *Phys. Rev. Lett.*, 1986, **56**, 1404–1407.

53 J. Liu, Y. Mudryk, J. D. Zou, V. K. Pecharsky and K. A. G. Jr, *J. Alloys Comp.*, 2014, **600**, 101–106.

54 H. Li, Y. Wu, Z. Guo, P. Luo and S. Wang, *J. Appl. Phys.*, 2006, **100**, 103908.

55 F. Hellman, D. R. Queen, R. M. Potok and B. L. Zink, *Phys. Rev. Lett.*, 2000, **84**, 5411–5414.